Materials Horizons

ROYAL SOCIETY OF CHEMISTRY

COMMUNICATION

View Article Online
View Journal | View Issue

Cite this: *Mater. Horiz.*, 2024, **11**, 1032

Received 20th September 2023,
Accepted 29th November 2023

DOI: 10.1039/d3mh01511d

rsc.li/materials-horizons

A responsive cascade drug delivery scaffold adapted to the therapeutic time window for peripheral nerve injury repair†

Yizhu Shan,‡[abc] Lingling Xu,‡[d] Xi Cui,[ac] Engui Wang,[a] Fengying Jiang,[ae] Jiaxuan Li,[a] Han Ouyang,[c] Tailang Yin,[f] Hongqing Feng,*[ac] Dan Luo,*[ac] Yan Zhang*[b] and Zhou Li *[ac]

Peripheral nerve injury (PNI) is a common clinical challenge, requiring timely and orderly initiation of synergistic anti-inflammatory and reparative therapy. Although the existing cascade drug delivery system can realize sequential drug release through regulation of the chemical structure of drug carriers, it is difficult to adjust the release kinetics of each drug based on the patient's condition. Therefore, there is an urgent need to develop a cascade drug delivery system that can dynamically adjust drug release and realize personalized treatment. Herein, we developed a responsive cascade drug delivery scaffold (RCDDS) which can adapt to the therapeutic time window, in which Vitamin B12 is used in early controllable release to suppress inflammation and nerve growth factor promotes regeneration by cascade loading. The RCDDS exhibited the ability to modulate the drug release kinetics by hierarchically opening polymer chains triggered by ultrasound, enabling real-time adjustment of the anti-inflammatory and neuroregenerative therapeutic time window depending on the patient's status. In the rat sciatic nerve injury model, the RCDDS group was able to achieve neural repair effects comparable to the autograft group in terms of tissue structure and motor function recovery. The development of the RCDDS provides a useful route toward an intelligent cascade drug delivery system for personalized therapy.

New concepts

In traditional drug cascade delivery systems, the release kinetics of the loaded drug are programmed and difficult to adjust in response to the patient's disease process. However, due to individual differences, the repair process in patients after nerve injury differs widely, and in particular the inflammatory stage experienced by each person is different. Therefore, an ideal cascade drug delivery system not only requires orderly and sustained release of drugs, but also needs to be able to adjust the release kinetics of multiple drugs according to the real-time inflammation situation of each patient, thereby flexibly adapting to the patient's therapeutic time window and achieving the best repair effect. Herein, we developed a responsive cascade drug delivery scaffold (RCDDS) adapted to the therapeutic time window for peripheral nerve injury repair through multiple-level encapsulation of VB_{12} and NGF. The RCDDS system can adjust the release kinetics of the two drugs through ultrasound stimulation according to the patient's disease-related indicators to meet the different requirements of the anti-inflammatory and nerve regeneration stages, facilitating the implementation of personalized treatment.

1. Introduction

Peripheral nerve injury (PNI) is a complex and challenging clinical condition that affects at least 2 million individuals worldwide. It can be caused by a variety of factors, including trauma, surgical complications or congenital defects. These injuries can lead to severe disabilities, pain, and sensory and motor defects, which can seriously impact the life quality of patients.[1] Despite tremendous strides in neuroscience over the past few decades, nerve injury remains one of the most challenging clinical conditions to cure due to the complex structure and function of the nervous system. The process of PNI includes a series of cascading processes that occur at the microscopic level. The first stage involves Wallerian degeneration and a local inflammatory

[a] *Beijing Institute of Nanoenergy and Nanosystems, Chinese Academy of Sciences, Beijing 100083, China. E-mail: zli@binn.cas.cn*
[b] *Department of Clinical Laboratory, Renmin Hospital of Wuhan University, Wuhan 430060, China*
[c] *School of Nanoscience and Engineering, Chinese Academy of Sciences, Beijing 100049, China*
[d] *CAS Key Laboratory for Biomedical Effects of Nanomaterials and Nanosafety & CAS Center for Excellence in Nanoscience, National Center for Nanoscience and Technology of China, Beijing 100190, China*
[e] *Center on Nanoenergy Research, School of Physical Science and Technology, Guangxi University, Nanning 530004, China*
[f] *Reproductive Medicine Center, Renmin Hospital of Wuhan University, Wuhan 430060, China*
† Electronic supplementary information (ESI) available. See DOI: https://doi.org/10.1039/d3mh01511d
‡ Y. S. and L. X. contributed equally to this work.

response that persists for approximately 5–7 days after the injury occurs.[2] During this stage, phagocytic neutrophils and macrophages are recruited to the injury site to remove cell debris, which lays the foundation for subsequent regeneration. However, if the inflammation is poorly controlled at this stage, glial scars will form, which impede axonal outgrowth and cause further damage to surrounding tissues.[3,4] Therefore, in the early stage of injury, administering a certain amount of anti-inflammatory drugs can help the following regeneration. The next stages involve cell proliferation, migration, and tissue remodeling. Axon regeneration begins at the proximal site and is characterized by the proliferation of Schwann cells (SCs) forming Büngner bands that guide the assembly and elongation of growth cones.[5] However, nerve cells have a limited ability to regenerate after injury, making it difficult for axons to grow through gaps in damaged nerves. In particular, when the gap between nerve injuries is significant, it will lead to insufficient nutrition inside the nerve, making it difficult to complete nerve regeneration. The sustained release of growth factors during this phase can effectively promote nerve repair.[6] In order to promote the process of nerve regeneration, neural scaffold implantation strategies have been proposed to effectively bridge the gap in damaged nerve tissue, which not only provide physical support but also can load therapeutic agents, creating an optimal three-dimensional environment for nerve repair.[7,8] Among all the scaffold materials, hydrogels exhibit some characteristics similar to native extracellular matrix (ECM), such as high water content, providing a suitable environment for cell growth and extension, a capacity for loading hydrophilic drugs or biological factors, and the ability to respond to external stimuli.[9,10] Currently the developed drug delivery neural scaffolds mainly focus on the delivery of a single type of drug.[11] But the regeneration process after nerve tissue injury is very complex, from the initial inflammatory response, cell recruitment, cell differentiation to tissue regeneration, usually involving multiple signalling molecules.[12] A single drug treatment cannot simultaneously regulate multiple different stages of nerve repair, thus resulting in suboptimal therapeutic effects. To improve the therapeutic effect of drug delivery neural scaffolds, it is necessary to design a cascading multi-drug combined delivery system that can release drugs in chronological order based on the repair process. It is worth mentioning that the drug release kinetics of traditional drug cascade delivery systems are uncontrollable. However, individual differences in patients mean the duration of repair processes after nerve injuries varies, especially the inflammatory stage. For patients with short inflammatory periods, using traditional drug cascade release systems may miss the optimal treatment opportunity due to failure in timely promoting the repair process. Therefore, an ideal cascade drug delivery system not only requires orderly and sustained release of drugs, but must also be able to adjust the release kinetics of multiple drugs through exogenous physical stimulation according to the real-time inflammatory conditions of each patient in order to accommodate the therapeutic time window of nerve repair.

In light of this consideration, we developed a responsive cascade drug delivery scaffold (RCDDS) adapted to the therapeutic time window for peripheral nerve injury repair (Scheme 1(A)).

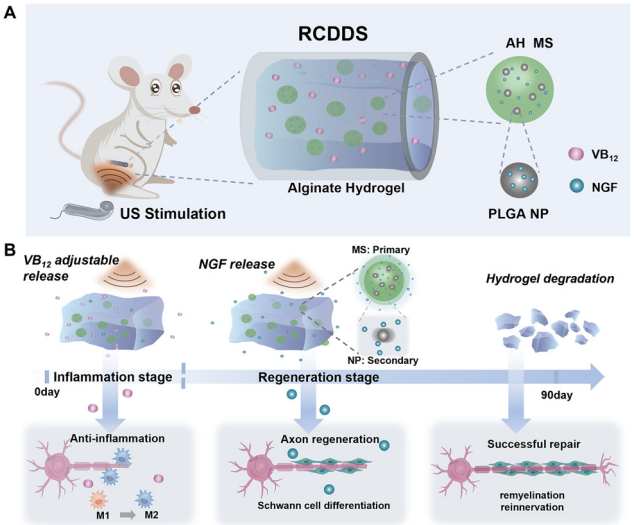

Scheme 1 Schematic illustration of the structure and drug release process of the responsive cascade drug delivery scaffold (RCDDS) for peripheral nerve injury repair. (A) A brief illustration of the structure of the RCDDS implanted in SD rat. (B) Drug release process of the RCDDS and the corresponding repair stage. Vitamin B_{12} loaded in the hydrogel system can be adjustably released in the early stage by ultrasound to alleviate inflammation, while NGF loaded in alginate microspheres and PLGA nanoparticles can be gradually released from the RCDDS to promote axon regeneration one month after implantation.

The main structure of the RCDDS was an ultrasound-responsive 2.5% calcium double-crosslinked alginate hydrogel (AH) network, whose hierarchical polymer networks could be sequentially opened under ultrasound stimulation (US). The RCDDS directly encapsulated with Vitamin B_{12} (VB_{12}, an indispensable nutrient to reduce neuroinflammation),[13,14] thereby alleviating inflammation in the early stage; at the same time, it also loads nerve growth factor (NGF, a thoroughly studied neurotrophin[15]) in a triple-encapsulated manner, *i.e.* NGF was first loaded into poly(lactic-*co*-glycolic acid nanoparticles) (PLGA NPs) then encapsulated into 5% alginate microspheres (MSs) and finally integrated within the RCDDS, for the long-term process of promoting nerve regeneration and reconstruction. It is worth mentioning that the RCDDS system can flexibly adjust the release kinetics of the two drugs through ultrasound stimulation according to the therapeutic time window for different individuals, so as to meet the different requirements of the anti-inflammatory and nerve regeneration stage, and facilitate the implementation of personalized treatment. In the RCDDS system, the loose structure of low concentration AH (2.5%) could respond rapidly to ultrasound, thereby realizing the burst release of VB_{12} regulated by ultrasonic power; the triple-encapsulation system and the dense structure of the high concentration MSs (5%) made the release of NGF slower than that of VB_{12}, and ultrasonic stimulation can regulate the drug release of NGF in a wider time period (Scheme 1(B)). The RCDDS were further implanted into the defected sciatic nerve rat model, and the two drugs were controlled on demand by ultrasonic stimulation with an adjustable power density according to the pathological conditions of the rats. The *in vivo* results proved the RCDDS combined

with tunable ultrasound stimulation promoted neural repair after PNI, both histologically and functionally. In general, we designed an ultrasound-responsive cascaded drug delivery system adapted to the therapeutic time window, ushering in a new era of personalized therapy for complex diseases with a multi-stage therapeutic process.

2. Results and discussion

2.1 Fabrication and characterization of the RCDDS

The fabrication of the RCDDS is a cascaded encapsulation process and is briefly illustrated in Fig. 1(A). The PLGA NPs were produced using an emulsifying-solvent evaporation technique and their regular structure was confirmed using transmission electron microscopy (TEM) imaging (Fig. 1(B)). The diameter of the NPs was estimated to be approximately 109.49 ± 2.46 nm using dynamic light scattering (Fig. 1(C) and Fig. S1, ESI†). Notably, the polymer dispersity index (PDI) value was found to be as low as 0.022, indicating a relatively narrow size distribution. Next, PLGA NPs with NGF molecules adsorbed on the surface were further loaded into alginate MSs using an electrospray system. The resultant MSs showed a monodispersed spherical morphology under a metallographic microscope and the average diameter was about 260.34 ± 21.25 μm (Fig. 1(D)). Successful encapsulation of the PLGA NPs was confirmed using scanning electron microscopy (SEM) (Fig. 1(E)).

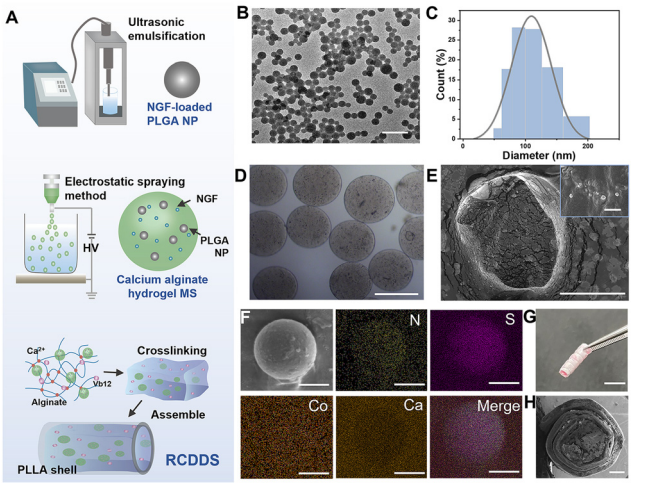

Fig. 1 Preparation and characterization of RCDDS. (A) Illustration of the preparation process of the RCDDS system. (B) Morphology of the NGF-loaded PLGA nanoparticles determined using TEM. The scale bar represents 500 nm. (C) DLS results of the size of NGF-loaded PLGA nanoparticles. (D) The photograph of alginate hydrogel microspheres taken using a metallurgical microscope. The scale bar represents 200 μm. (E) The sectional view of the prepared microspheres and the larger version of the internal structure of the encapsulated PLGA nanoparticles. The scale bar represents 200 μm at low magnification and 300 nm at high magnification. (F) EDS results of one of the microspheres loaded in the calcium cross-linked alginate hydrogel. The elements of N, S, Co, and Ca and a merged image are shown. The scale bar represents 100 μm. (G) A picture of the RCDDS in which the hydrogel is filled into the preformed PLA porous shell. The scale bar represents 500 μm. (H) A side view picture of the RCDDS obtained using SEM. The scale bar represents 500 μm.

VB_{12} and NGF-loaded MSs were further mixed in calcium cross-linked alginate hydrogel to form the RCDDS (Fig. S2, ESI†). The energy dispersive spectrometer (EDS) results showed the RCDDS was successfully loaded with two drugs, as shown in Fig. 1(F). The elements N and S were distributed mainly in the spherical MSs which indicated the existence of the protein drug – NGF. Since VB_{12} is a polycyclic compound containing trivalent cobalt, the uniformly dispersed Co element represented the successful doping of VB_{12} in AH. The calcium signal confirmed the successful construction of the ionically cross-linked structure in the AH. With the aim of stabilizing the structure of the drug-loaded hydrogel to form an implantable neural scaffold, AH loaded with VB_{12} and NGF was further encapsulated in the preformed PLLA porous shell to form RCDDS (Fig. 1(G)). The encapsulated core–shell structure was verified using cross-sectional SEM (Fig. 1(H)).

2.2 RCDDS possessed tunable drug release kinetics under different power ultrasound stimulation

The main component of the RCDDS is AH, a network structure formed by cross-linking of calcium ion and sodium alginate. For implantable biomaterials, stress matching is an important parameter to consider. Before exploring the ultrasound responsiveness of the RCDDS, we first tested the influence of different ratios of alginate and calcium on the modules and rheological characterizations of hydrogels (Fig. S3, ESI†). With the increase of sodium alginate concentration, the values of storage modulus (G') and loss modulus (G'') increased, indicating that the degree of crosslinking between hydrogel networks increased and the hydrogel becomes harder. Through the compression test of the hydrogels, the Young's modulus of 2.5% alginate was similar to that of nerve tissue, which is more suitable for nerve repair.[16] Fourier transform infrared spectroscopy (FTIR) and thermogravimetric analysis-differential scanning calorimetry (TG-DSC) was further adopted to analyse the composition of the scaffold, and the results are shown in Fig. S4 (ESI†). In the FTIR results, we found that the RCDDS had a characteristic absorption peak at ~1490 cm^{-1}, which was mainly attributed to the stretching vibration of the carbonyl group (C═O) in the protein, indicating the successful loading of NGF. Furthermore, we also found that the RCDDS possessed characteristic absorption peaks near 1360 cm^{-1}, which were assigned to the coupled vibrations in the corrin ring of VB_{12}, proving the existence of VB_{12}. Thermogravimetric analysis showed that the first weight loss occurred at 100 °C, which was mainly due to the sharp drop in the weight of the system caused by the evaporation of water in the alginate hydrogel. Next, the decomposition of alginate resulted in a slow decrease in the weight of the system. We also evaluated the cell compatibility of different concentrations of alginate hydrogel. L929 cells were seeded on the hydrogels and confocal images of phalloidine and 4′,6-diamidino-2-phenylindole (DAPI) were taken after co-culture for a period of time (Fig. S5, ESI†). The three-dimensional images showed that the depth of cell infiltration on the 1% and 2.5% AH were higher than that on a common tissue cell plate (TCP). Although deeper cellular migration could be observed on 5% alginate hydrogel, the cells could not stretch and grow which indicated poor cell

viability. Taking into account both the modulus and co-culture condition of cells, we chose the 2.5% alginate hydrogel for the subsequent experiment.

The RCDDS possessed an ultrasound-tunable micro/nano structure. The calcium-dependent cross-linked network in the alginate hydrogels, as the main component of the RCDDS, would be opened under ultrasound stimulation, thereby forming a porous structure and accelerating the release of drugs encapsulated in the hydrogels (Fig. 2(A) and Fig. S6, ESI†). We applied a series of ultrasound intensities to the RCDDSs and froze them immediately to maintain their morphologies and determine the influence of ultrasound stimulation on the RCDDS structure (Fig. 2(B)). In the absence of ultrasound, the hydrogel showed a complete structure; and as the intensity of the ultrasound increased, the pores of the hydrogel became larger and more numerous. In addition, the multilevel encapsulation structure of the RCDDS also provides it with the potential for cascading drug release, as shown in Fig. 2(C). As a drug regulating the inflammation and immune microenvironment, VB_{12} was directly loaded into the AH network of the RCDDS for early release in nerve injury to control excessive inflammation and prevent glial scar formation. NGF, as a pro-regenerative molecule, should be released during the repair process to accelerate regeneration. Therefore, NGF-loaded PLGA NPs were first encapsulated in MS microspheres and then embedded into the RCDDS. This multilevel encapsulation strategy enabled NGF to be released later than VB_{12}, and this slow delivery could be maintained for nearly a month.

In view of the combination of ultrasonic responsiveness and cascading drug release ability, the RCDDS can regulate

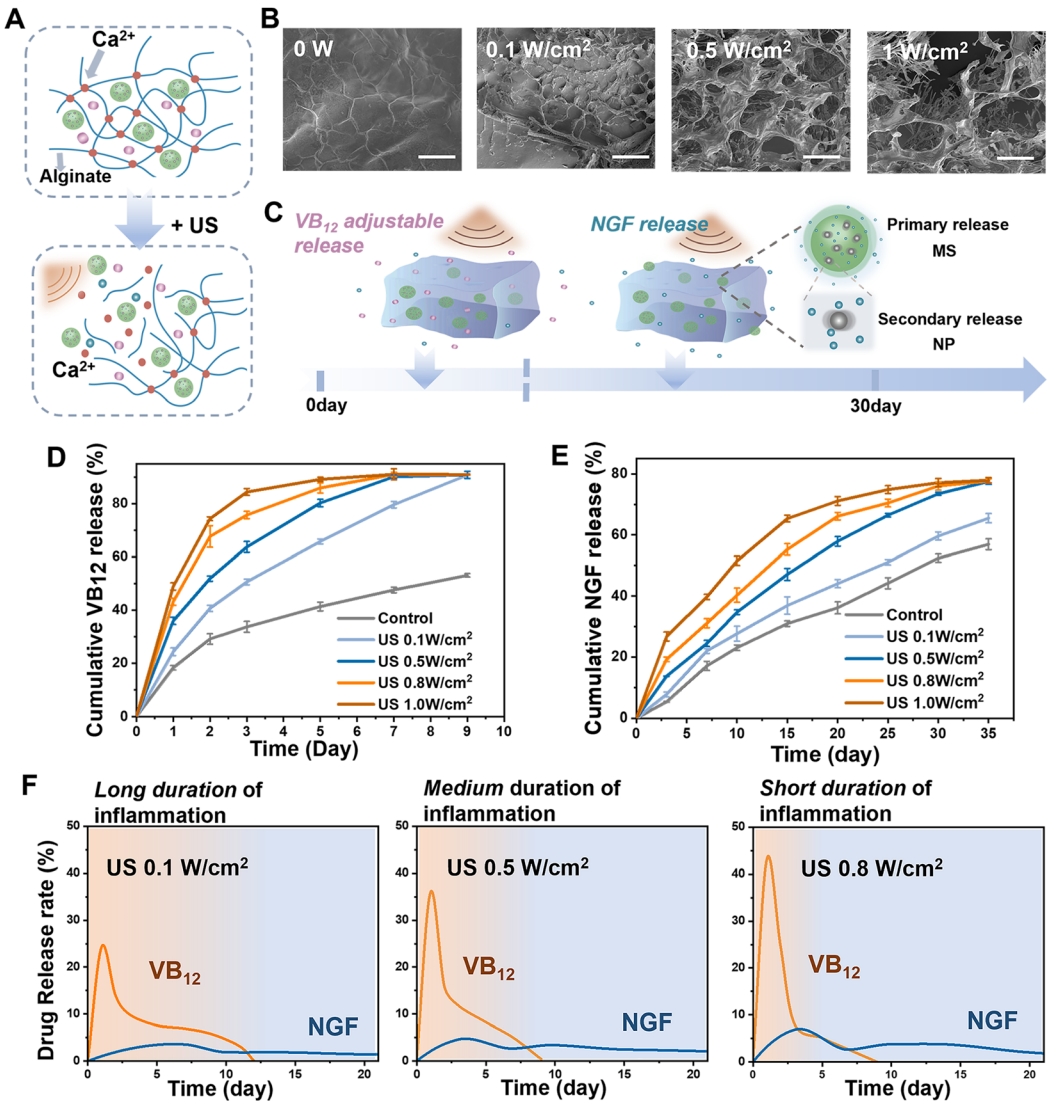

Fig. 2 Drug release *in vitro*. (A) Schematic diagram of the mechanism of ultrasound-responsive calcium cross-linked alginate hydrogel. (B) Morphological changes of the hydrogels under different ultrasonic intensities. The scale bar represents 50 μm. (C) Timeline and drug release behavior of the RCDDS. (D) The cumulative release curves of VB_{12} from the RCDDS under different intensities of ultrasound stimulation. (E) The cumulative release curves of NGF tested using an Elisa kit under different intensities of ultrasound stimulation. (F) Three different release kinetics of VB_{12} and NGF that can correspond to different durations of inflammation under different intensities of US.

the release kinetics of both drugs by applying exogenous ultrasonic stimulation, thereby adapting the therapeutic time window of anti-inflammation and nerve regeneration. When different intensities of ultrasound were applied to RCDDS, the *in vitro* drug release kinetics of VB_{12} and NGF were systematically evaluated. Compared with the sample without ultrasound stimulation, the VB_{12} release rates were greatly accelerated after application of US. The release of VB_{12} under 0.8 W cm^{-2} US for 1 min per day was so rapid that 85% of loaded VB_{12} was depleted within 3 days, realizing a short course of anti-inflammatory therapy. However, under 0.1 W cm^{-2} US, the release of VB_{12} could last for 12 days to achieve long-term anti-inflammatory treatment. The administration of 0.5 W cm^{-2} US achieved a moderate course of anti-inflammatory treatment, with stable release of VB_{12} within 7 days (Fig. 2(D)). Similar to VB_{12}, the release kinetics of NGF was also modulated by using different ultrasound power density (Fig. 2(E)). Short (20 days) and long (more than 35 days) courses of nerve repair treatment with US at 0.8 W cm^{-2} and 0.1 W cm^{-2}, respectively, were carried out. The RCDDS could release NGF continuously and smoothly for 35 days under US at 0.5 W cm^{-2}. In order to more intuitively demonstrate the responsiveness of the system to different ultrasound intensities, we statistically analyzed the average single drug release rates from the first three days, and the results showed that the release rates of both VB_{12} and NGF increased with the increase of ultrasound intensities (Fig. S7, ESI†). The RCDDS, unlike in the traditional cascade drug delivery system that releases drugs invariably, can instead adapt to the therapeutic time window with ultrasound to better target patients with different disease progress (Fig. 2(F)). For example, in the case of long-lasting inflammation, 0.1 W cm^{-2} ultrasound can be used to slowly open the polymer chain of the RCDDS, and achieve long-term anti-inflammation by prolonging the release time of VB_{12}. For patients with a shorter inflammatory period, higher power ultrasound stimulation (such as 0.8 W cm^{-2}) can be used to shorten the anti-inflammatory treatment and quickly enter the next stage of nerve regeneration. In addition, different ultrasound intensity patterns can also adjust the treatment time of nerve repair to achieve a better personalized treatment effect.

2.3 *In vitro* assessment of the neuroregenerative potential of RCDDS

Before using the RCDDS in animal experiments, we evaluated the biocompatibility of RCDDS and the potential side effects of ultrasound stimulation on cells *via* live/dead cell staining. PC12 cells were chosen due to their easy availability and similar morphology to neurons. After cultivating with RCDDS and applying a certain intensity of US every day for 3 days, different visual fields were randomly selected to calculate the number of live and dead cells (Fig. 3(A)). The cell viability on TCP and the RCDDS were 98.2% and 98.9%, respectively; in addition, the cell viability of the RCDDS combined with 0.1 W cm^{-2}, 0.5 W cm^{-2}, and 0.8 W cm^{-2} US groups were also not significantly different from that of the RCDDS group. However, a higher ultrasound intensity (*e.g.*, 1 W cm^{-2}) resulted in a decrease in cell activity (Fig. S8, ESI†). The results suggest that the RCDDS has good biocompatibility and a moderate intensity of US does not affect cell viability.

PC12 cells can be induced by nerve growth factor to differentiate into neuronal like cells, growing axons that are similar in structure and function to neuronal cells.[17] We tested the potential of the RCDDS to induce axon growth in PC12 cells *in vitro*. The cells were divided into four groups including the TCP (control), RCDDS group, ultrasound stimulation-only group (US) and RCDDS combined with 0.5 W cm^{-2} US groups, respectively. After five days of co-culture, fluorescent images of the cytoskeleton and nucleus staining showed that compared with the control group, cells in the RCDDS + 0.5 W cm^{-2} US group exhibited obvious axonal sprouts with a length of 44.463 ± 12.967 μm (Fig. 3(B)). In the absence of ultrasonic stimulation, the RCDDS was not able to release a sufficient dose of NGF, and the axon length of the RCDDS has no significant difference with the control group. For the experimental group with only ultrasound stimulation and no drug loading, ultrasound stimulation can also promote the growth of axons to a certain extent, because ultrasound can regulate the neuroplasticity and promote the secretion of neurotrophin. The ability of the RCDDS to induce PC12 cells to differentiate into neuron-like cells under ultrasound stimulation at different power densities was further investigated (Fig. S9, ESI†). In the RCDDS combined with 0.1 W cm^{-2} or 0.8 W cm^{-2} US groups, the axon lengths grown by the PC12 cells were 43.371 ± 5.126 μm and 43.828 ± 7.907 μm, respectively, which were not significantly different from that of the RCDDS + 0.5 W cm^{-2} US group. This is due to the fact that although ultrasound changed the duration of NGF release, the difference in NGF concentration at different power densities was not significant and was within the effective range of the drug, so it would not cause an obvious difference in curative effect. However, under 1 W cm^{-2} ultrasonic stimulation, the cells presented an abnormal aggregation state, because the high intensity of ultrasonic power intensity affected the cell viability.

2.4 The RCDDS presented a powerful anti-inflammatory ability both *in vitro* and *in vivo*

VB_{12}, as an indispensable nutrient for maintaining the physiological function of the nervous system, participates in the synthesis of lipoproteins in nerve tissue, and protects the physiological metabolism and function of the nerve myelin sheath. It has been proved that VB_{12} is able to scavenge reactive oxygen species (ROS) at the injury site,14 thereby reducing the expression of proinflammatory cytokines and increasing anti-inflammatory cytokines, which ultimately contributes to the alleviation of Wallerian degeneration and neuroinflammation.[18–21] Compared to classic anti-inflammatory drugs, such as steroidal anti-inflammatory drugs (dexamethasone) and non-steroidal anti-inflammatory drugs (aspirin), VB_{12} is an endogenous nutrient with mild anti-inflammatory effects, which has fewer side effects and a wider range of safe dosages.[21–24] To validated whether the drug release system of the RCDDS can alleviate excessive ROS *in vitro*, we established an LPS-induced

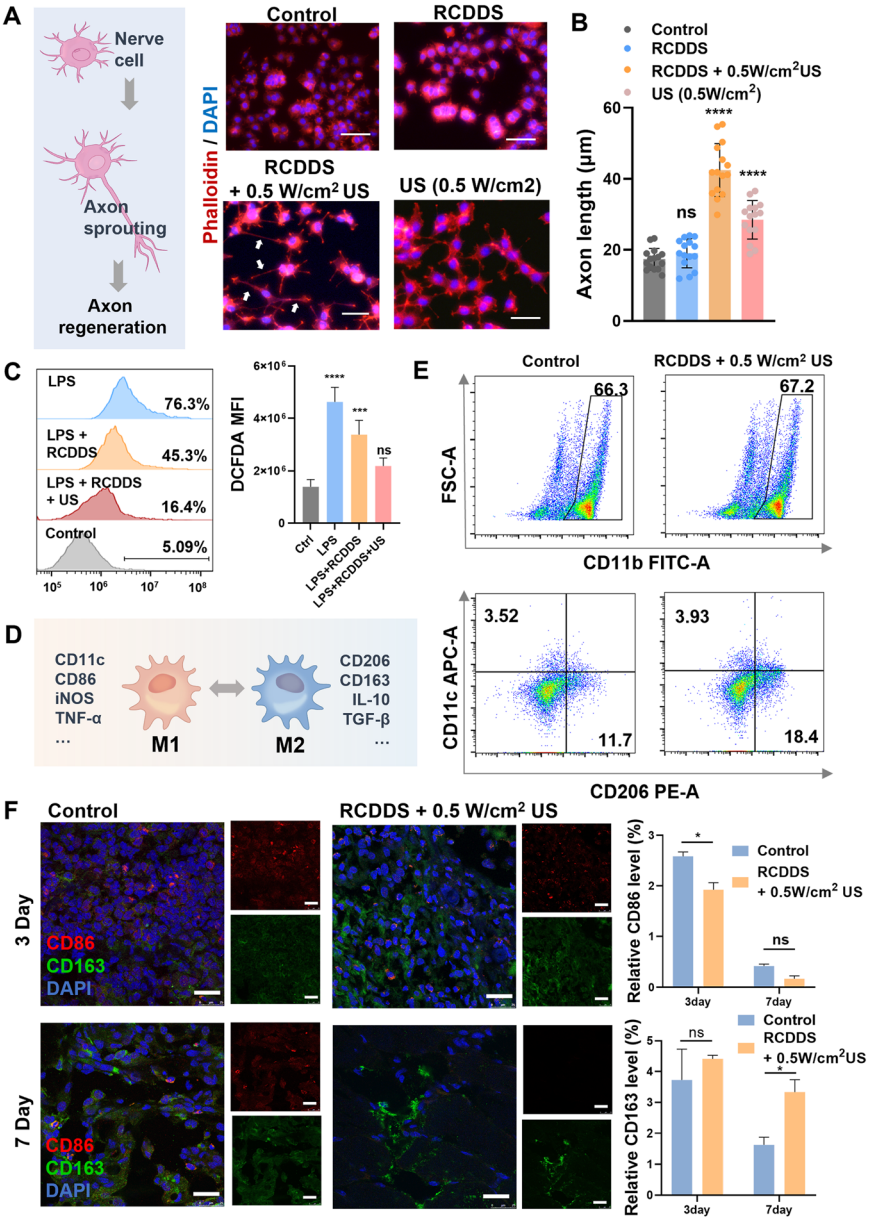

Fig. 3 Neuroregeneration and anti-inflammation evaluation *in vitro* and *in vivo*. (A and B) Cytoskeleton staining of PC12 cells cultured with TCP or RCDDS and the different intensity of ultrasound stimulation for 5 days. The scale bar represents 50 μm. The statistical data showed the axon length of PC12 cells of the different groups (n = 15). (C) The flow cytometry results of the effect of the RCDDS on cellular ROS levels. (D) Schematic diagram of the transformation into M1 type macrophages and M2 type macrophages and the corresponding markers and cytokines. (E) Representative flow cytometry plots and statistical data of $CD11b^+$, $CD11c^+$, $CD206^-$ macrophages (M1) and $CD11b^+$, $CD11c^-$, $CD206^+$ macrophages (M2) polarization in the control and RCDDS + 0.5 W cm^{-2} US group on days 7 in mice (n = 4). (F) Representative immunostaining and statistical data of CD86 and CD163 macrophages 3 days and 7 days after implantation near the mouse sciatic nerve (n = 3). The scale bar represents 25 μm at low magnification and 25 μm at high magnification.

inflammatory model in RAW 264.7 cells. The results showed that the ROS level decreased significantly in the group of RCDDS + 0.5 W cm^{-2} US compared with the LPS-induced inflammation group. Compared with the blank group without LPS induction, there was no statistical difference in the average fluorescence intensity statistics of ROS in cells in the RCDDS + 0.5 W cm^{-2} US group, confirming that the VB_{12} released by the RCDDS effectively suppressed inflammation (Fig. 3(C)).

Macrophages play a crucial role in the inflammatory response process which are recruited to the nerve injury site within hours after injury.[25] Macrophages not only remove myelin fragments through phagocytosis, but also secrete many biologically active cytokines, which play a key role in regulating nerve regeneration. Macrophages can be divided into M1 (pro-inflammatory) and M2 (anti-inflammatory) phenotypes (Fig. 3(D)). M1 macrophages can secrete inflammatory cytokines like iNOS and TNF-α and their typical markers are CD11c and CD86; while M2 macrophages reduce inflammation and promote regeneration by secreting anti-inflammatory cytokines like IL-10 and TGF-β, and their typical markers are CD206 and CD163.[26,27]

Modulating the polarization of macrophages towards the M2 phenotype is critical for nerve injury repair as it improves the inflammatory immune microenvironment and accelerates tissue repair. To further verify the anti-inflammatory effect of RCDDS *in vivo*, we established a mouse model of nerve injury to observe the phenotype conversion of macrophages in different periods. After the transection of sciatic nerve and the implantation of RCDDS in mice, we conducted US stimulation every day on the mice in the RCDDS + 0.5 W cm^{-2} US group while the control group underwent transection surgery only. The tissues surrounding the implant site were isolated for flow cytometry at 7 days after treatment. The data in Fig. 3(E) indicated that the macrophage level ($CD11b^+$) in the RCDDS + US group was similar to that in the control group, but there were more M2 type macrophages ($CD206^+$, $CD11c^-$) (18.4%) in the RCDDS + 0.5 W cm^{-2} US group than in the control group (11.7%). This level is comparable to the significant reduction in inflammation observed in a study by Zhang's group.[28] As shown by the immunofluorescence staining of tissue sections, both the treatment group and the control group exhibited high levels of M1 type macrophages ($CD86^+$ signal) at three days, mainly due to the nerve injury. After seven days, although the levels of M1 type cells in both groups were close and very low, the macrophages in the treatment group mainly shifted to the M2 type, as evidenced by higher levels of $CD163^+$ in the treatment group compared to the control group (Fig. 3(F)). These findings suggest that the RCDDS has inflammation regulating effects at the early stage of nerve injury.

2.5 The RCDDS promoted remyelination and axon outgrowth

Different kinds of nerve scaffolds were implanted into the site of a 10-mm defect in the static nerve of the right leg of SD rats for evaluation of the treatment effect of the RCDDS and a schematic of the timeline for the animal experiment is shown in Fig. 4(A). The animals were randomly divided into six different groups: autograft (positive control), AH scaffold loaded with single drug VB_{12} combined with 0.5 W cm^{-2} US stimulation (AH_{VB12} + US), NP-MS-AH triple encapsulated NGF scaffold combined with 0.5 W cm^{-2} US stimulation (NP-MS-AH_{NGF} + US), a cascade drug delivery system loaded with VB_{12} and NGF simultaneously without an ultrasound-controlled drug therapy window (RCDDS), RCDDS combined with fixed US stimulation (0.5 W cm^{-2}) (RCDDS + US) and RCDDS combined with tunable US stimulation (RCDDS + tun-US). In the RCDDS + tun-US group, we dynamically adjusted the ultrasound intensity according to the changes in the physiological indicators of the rats, thereby altering the release kinetics of the anti-inflammatory/nerve regenerative drugs so as to facilitate the timely entry into different treatment stages according to the disease conditions. For example, for the anti-inflammatory treatment stage, we assessed the level of inflammation after nerve injury in rats by detecting the level of inflammatory cells in the blood, especially focusing on the number of monocytes and neutrophils (Fig. S10, ESI†). Neutrophils, a marker of acute inflammation, are rapidly mobilized and able to function rapidly after injury; while monocytes, as a marker of chronic inflammation, often appear 48 hours after injury and develop in the next few days or even play a major role within a few weeks.[29] During the inflammatory phase, moderate-intensity ultrasound stimulation was used to prolong the release of VB_{12} and achieve sustained anti-inflammatory therapy. When the detection of blood biochemical indicators (neutrophil and monocyte levels) confirmed that the inflammation level of the rats tended to be normal, we increased the ultrasound intensity to promote the rapid release of VB_{12}, and then entered the next stage of repair treatment in time.

At 12 weeks post-transplantation, the sciatic nerves of all the groups were isolated for morphology assessment. Longitudinal sections of the regenerated nerves were stained with neuronal marker NF200, Schwann cell marker S100 and DAPI (Fig. 4(B)). The new-grown nerve fibers and the Schwann cell encapsulation indicate the successful regeneration of nerve morphologically. Among all groups, RCDDS + tun-US presented the densest nerve fibers ($NF200^+$ 27.07 ± 0.92%) and the greatest amount of Schwann cell encapsulation ($S100^+$ 28.75 ± 0.94%) which showed no significant difference in the autograft group ($NF200^+$ 27.53 ± 0.58%, $S100^+$ 29.82 ± 0.22%). Moreover, nerves in the (RCDDS + tun-US) group displayed more continuous morphology and a higher density than the other groups. These results demonstrate the unique advantages of the cascade drug delivery scaffold in the anti-inflammatory and repair stages (Fig. 4(B)–(D)).

In addition, based on the characterization of regenerated nerve myelin sheath using TEM, we further discovered the therapeutic effects of different drug delivery paradigms on the morphological recovery of the injured nerve. TEM images of the cross sections of regenerated sciatic nerves, shown in Fig. 4(E), exhibit more details of nerve fiber myelination and axonal maturity. The fact that the thickness of the myelin sheath of the nerves in the RCDDS + US group (665.68 ± 69.83 nm) is higher than those in the AH_{VB12} + US (394.08 ± 71.24 nm) and NP-MS-AH_{NGF} + US (519.71 ± 90.05 nm) groups suggests that the dual-drug cascade administration was more effective. Although the RCDDS group was also loaded with two drugs, the polymer chains could not be effectively opened due to the lack of ultrasonic stimulation, which reduced the local concentration of the drug and was not conducive to the formation of myelin (417.90 ± 104.23 nm) and the maturation of axons. The thickness of myelin in the RCDDS + US group was less than that of the RCDDS + tun-US group (771.47 ± 104.69 nm) due to the fact that the RCDDS + US group used ultrasonic stimulation at a fixed power density, and therefore the drug release behaviour was invariable, and these programmed anti-inflammatory and restorative treatments may not necessarily meet the optimal timing of the treatment. Among all groups, the RCDDS + tun-US group showed the densest nerve fibers and the largest amount of Schwann cells encapsulation. Altogether, the morphological assessment of the RCDDS + tun-US group was comparable to that of the autograft group (Fig. 4(B)–(G)), which is the gold standard of PNI repair. The above results confirm that the responsive cascade drug delivery system achieved excellent efficacy through on-demand drug delivery.

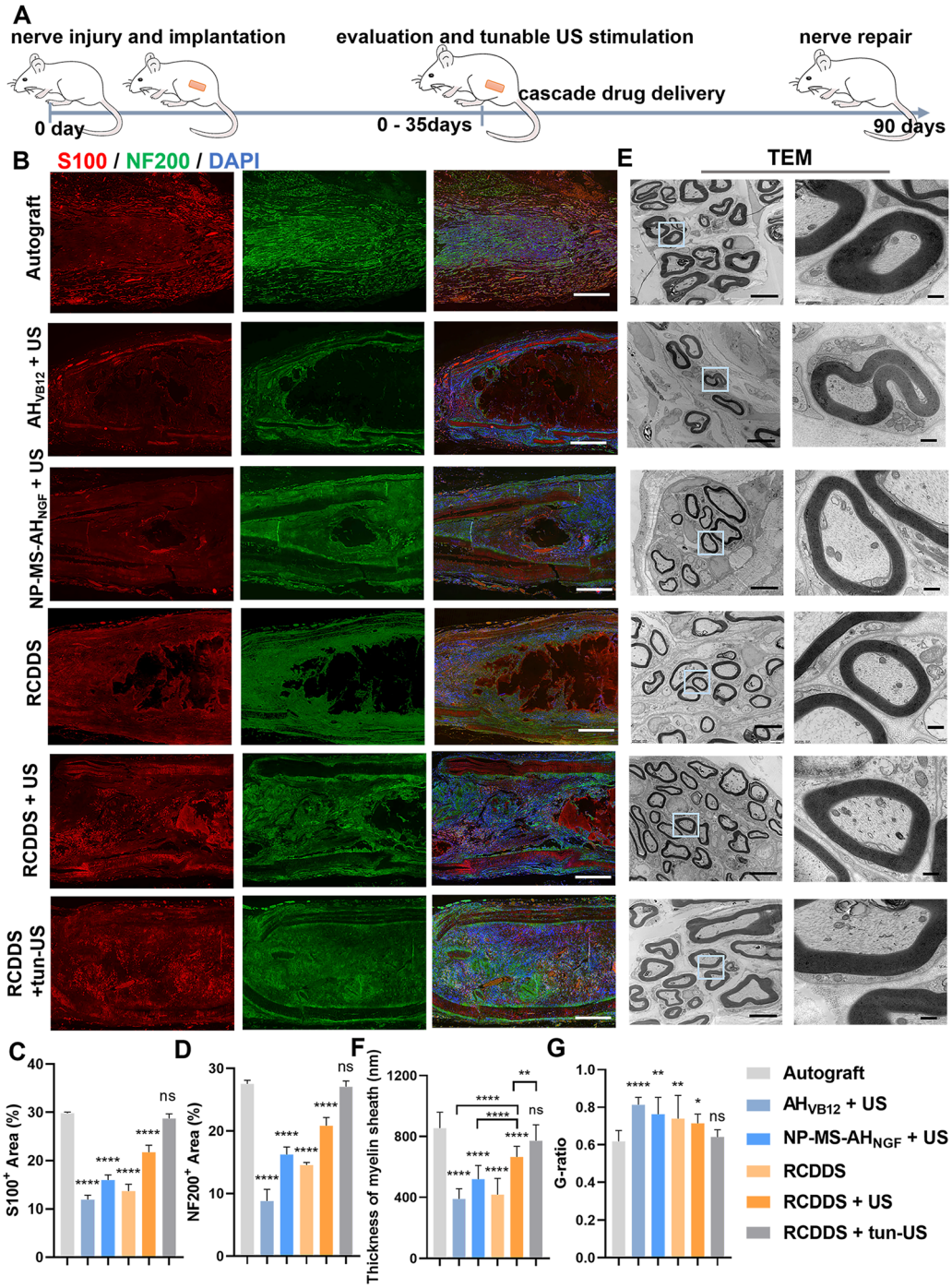

Fig. 4 Nerve repair morphology assessment after the RCDDS treatment. (A) Timeline of the animal experiment. (B) Fluorescence photographs of the longitudinal section of the sciatic nerve of the autograft, AH_{VB12}, NP-MS-AH_{NGF} + US, RCDDS, RCDDS + US and RCDDS + tun-US groups after 12 weeks post-implantation. The red is astrocyte marker S100 and the green is neuronal marker NF200. The scale bar represents 500 μm. (C) and (D) Analysis of the $S100^+$ and $NF200^+$ area in the six groups (n = 3). (E) Representative TEM images of the myelinated axonal regrowth in the six groups. The scale bar represents 4 μm at low magnification and 400 nm at high magnification. (F) Quantitative analysis of the thickness of the myelin sheath (n = 20). (G) Quantitative analysis of the G-ratio (n = 8).

2.6 The RCDDS achieves post-injury neurological recovery comparable to autografts

In addition to anatomical evidence, recovery of neural and muscle function is a direct indicator of PNI repair. The evaluation of functional recovery was conducted through an electromyography test, gastrocnemius muscle evaluation, and walking track analysis at the 12th week post-implantation. By electrically stimulating the nerves, the electrical signals are transmitted to the innervated muscle tissue to generate compound motor action potentials (CMAP) to reflect the condition of nerve damage and repair. The representative CMAP waveforms of all six groups and the statistical analysis of the CMAP amplitude

are shown in Fig. 5(A) and Fig. S11 (ESI†). Though the RCDDS + US group showed a higher amplitude of CMAP (3.35 ± 0.14 mV) compared to the middle three groups, there were still differences compared to the active control group (Autograft, 4.19 ± 0.18 mV). The amplitude of CMAP in the (RCDDS + tun-US) group was 3.84 ± 0.11 mV, which had no significant difference compared to that of the autograft group (4.19 ± 0.18 mV). In addition, we recorded the footprints of rats at the 6th, 8th, 10th, and 12th week after implantation to determine the static function index (SFI) of all groups (Fig. 5(B) and (C)). The SFI indexes of all the groups dropped dramatically after nerve injury. At each time point, the SFI of the (RCDDS + tun-US) group was very close to that of the autograft group which indicated that RCDDS with tunable US stimulation could better promote the functional recovery after nerve injury.

PNI can cause atrophy of the innervated muscles, while nerve repair can promote gradual muscle recovery. Muscle recovery was evaluated through analysis of the gastrocnemius muscles in each group. Briefly, at the 12th week post-implantation, the left and right gastrocnemius muscles of the rats in each group were dissected and weighted (Fig. 5(C)). The muscle weight recovery rate in the (RCDDS + tun-US) group was higher (89.12 ± 1.25%) than in the (AH_{VB12} + US) group (43.06 ± 5.97%), (NP-MS-AH_{NGF} + US) group (66.45 ± 2.85%), RCDDS group (43.70 ± 6.65%) and (RCDDS + US) group (79.84 ± 3.57%), and had no significant difference to the autograft group (92.64 ± 2.55%) (Fig. 5(D)). Masson staining of the right gastrocnemius muscles was also conducted to analyse the collagen fiber deposition and muscle fibrosis to evaluate the condition of muscle atrophy (Fig. 5(E) and (F)). The average

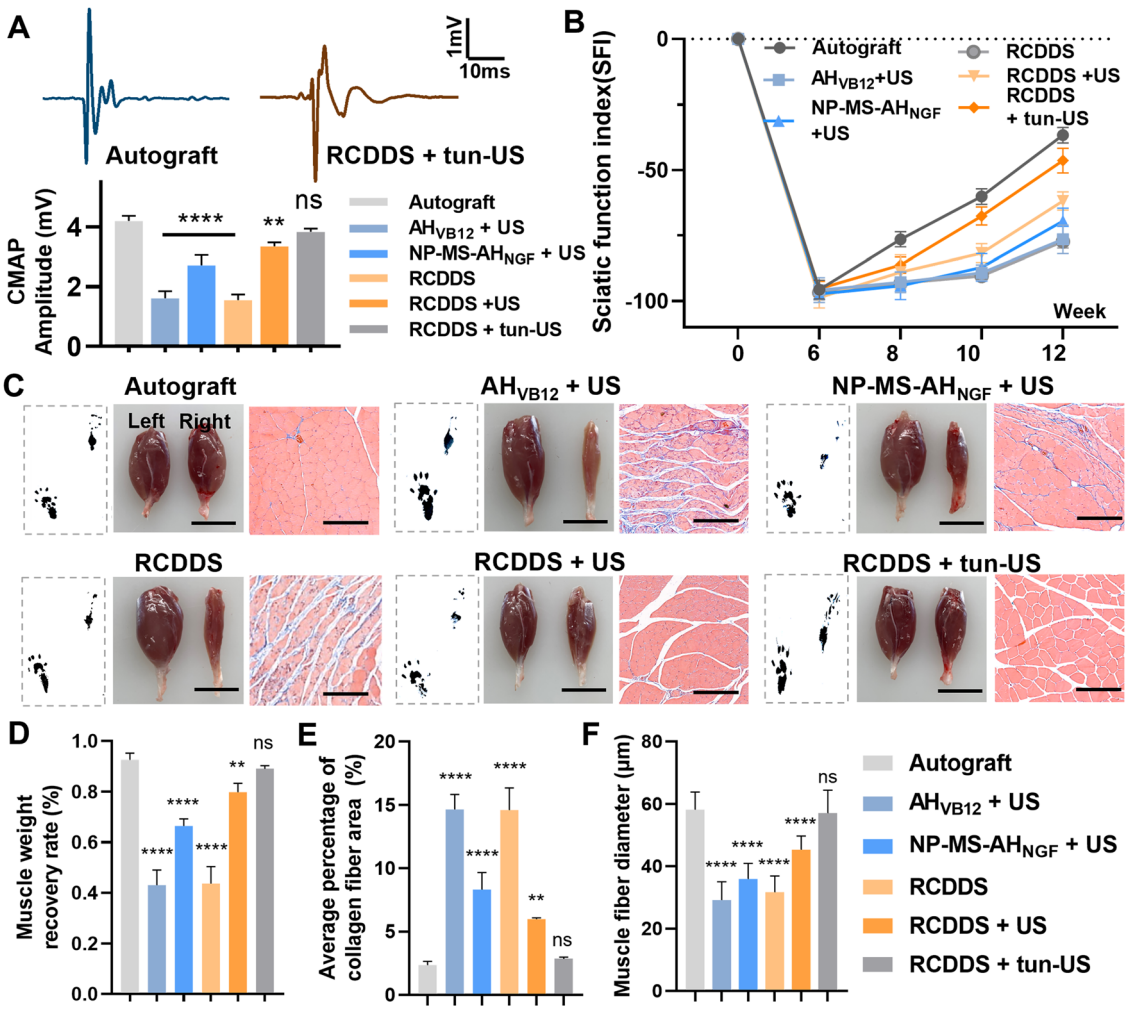

Fig. 5 Evaluation of the functional recovery with RCDDS treatment. (A) Representative CMAP at 12 weeks after implantation of the autograft and RCDDS + tun-US groups. The statistical data showed the average CMAP amplitude of the autograft, AH_{VB12} + US, NP-MS-AH_{NGF} + US, RCDDS, RCDDS + US and RCDDS + tun-US groups (n = 3). (B) The changing curve of the SFI index at 6, 8, 10 and 12 weeks of the six groups (n = 3). (C) Representative footprints, gastrocnemius muscles of the rats in six groups and Masson staining results of the right gastrocnemius muscle of each group. The scale bar represents 2 cm for the muscle pictures and 200 μm for the Masson staining images. (D) Statistical results of the muscle weight recovery rate (weight of the right gastrocnemius muscle/weight of the left gastrocnemius muscle) of each group (n = 3). (E) Quantitative analysis of the average percentage of collagen fiber area of Masson staining (n = 3). (F) Quantitative analysis of the muscle fiber diameter of Masson staining of each group (n = 3).

percentage of the collagen fiber area was calculated using ImageJ to assess the degree of muscle fibrosis. Compared to other treatment groups, significant decreased fibrosis in the (RCDDS + tun-US) group was observed, which was closest to the autograft group. Taken together, treatment with RCDDS and tunable US stimulation is very effective to alleviate denervation-induced muscle atrophy and restore nerve function.

3. Discussion

To address the complexity of neural repair processes, it is necessary to develop a multi-level and cascade drug delivery system in accordance with the repair process. Different drugs can work at different stages to achieve better regenerative effects. In this study, we mainly focus on the two main processes of nerve repair, inflammation and regeneration. Inflammation occurs at the beginning of nerve injury, lasts around 7 days, and features Wallenrian degeneration and a local inflammatory response. If the inflammation is poorly controlled at this stage, glial scars will form and inhibit nerve regeneration. The subsequent phase of neural regeneration is marked by cell proliferation, migration, and tissue remodeling, often lasting from three weeks up to months.[1] Neurotrophins, including brain-derived neurotrophic factor (BDNF), glial cell line-derived neurotrophic factor (GDNF) and NGF are widely used to promote axonal sprouting and functional recovery at the injury site.[30–32]

In our study, VB_{12} and NGF were chosen as the anti-inflammatory and pro-regeneration drugs. To enable the early release of VB_{12} to attenuate the post-injury inflammatory response, they were directly loaded into AH. As the inflammatory phase after nerve injury varies from patient to patient, we utilized ultrasound stimulation to modulate the kinetics of delivered drugs for on-demand dosing. By monitoring the patient's inflammatory indicators, different ultrasound power densities were used to adapt to the therapeutic time window by opening the cross-linked network of the hydrogel. The experimental results indicate that the controllable released VB_{12} reduced the degree of inflammation in the PNI site by reducing the local ROS level and inducing macrophages to transform into anti-inflammatory M2 type cells. In order to better achieve nerve repair after the anti-inflammatory stage, NGF was loaded in a triple-encapsulated manner, which ensured that the release of NGF was later than that of VB_{12}. The release kinetics of NGF was also controlled by ultrasound, and the NGF treatment period can be adjusted according to the patient's nerve repair condition.

Ultrasound can play a beneficial role in two aspects in our designed system. The first effect is ultrasound-responsive drug delivery. Ultrasound can open the double crosslinked network of hydrogels, leading to the gradual release of drugs in the calcium crosslinked network.[33] By adjusting appropriate ultrasound intensity, ultrasound-controlled drug release can avoid excessive local drug concentration or failure to reach an effective dose. Another function of ultrasound is its neuromodulation effect toward injured nerves.[34] Studies have shown that ultrasonic stimulation can promote the branching and growth of injured neurite, and protect the neurons from cell death, thereby accelerating nerve regeneration and slowing down denervated muscle atrophy and degeneration.[35] In addition, ultrasound stimulation can enhance the secretion of endogenous neurotrophin and improve the function of the factor.[36,37] Therefore, we can predict that the ultrasound we imposed can not only directly promote the regeneration of damaged neurons but also further accelerates nerve regeneration by promoting the release of exogenous NGF and the secretion of endogenous neurotrophins.

In the field of tissue engineering, the repair process of many tissue injuries is complex and requires phased and personalized treatment. We anticipate that this simple and effective drug delivery system can be further expanded and applied to the treatment of various diseases. For example, bone repair undergoes the initial inflammatory stage, proliferative stage, and remodeling stage.[38] A cascade drug delivery system for each bone repair stage can better promote the process of bone regeneration. Additionally, the RCDDS can also flexibly regulate the drug delivery rate to achieve on-demand personalized medication, thereby improving drug efficacy while reducing toxic side effects. In the future, this responsive cascade drug delivery scaffold can be further combined with ultrasound imaging drugs to achieve integrated diagnosis and treatment by dynamically monitoring drug release.

It is worth mentioning that all the materials we use in the RCDDS have good biocompatibility and are FDA approved materials, and these materials, especially alginate hydrogels, can degrade slowly with the treatment cycle.[39,40] These basic characteristics lay the foundation for the clinical transformation of RCDDSs.

4. Conclusions

In summary, we constructed a responsive cascaded drug delivery hydrogel scaffold (RCDDS) adapted to the therapeutic time window, whose cross-linked network could be opened to different degrees under different ultrasonic power densities, thereby regulating the release kinetics of VB_{12} and NGF. In animal models, we preliminarily verified the superiority of the RCDDS combined with tunable ultrasound stimulation in the treatment of nerve injury, which achieved excellent results comparable to autografts in terms of histology and functional recovery. Different from the traditional cascade drug delivery system, RCDDS can well adapt to the therapeutic time window of the drug according to the patient's pathological indicators and realize on-demand drug delivery, which will have great application potential in the personalized treatment of complex diseases in the future.

5. Materials and methods

Materials

Alginate, PVA (0588 low-viscosity), hexafluoroisopropanol, azo dimethylformamide and calcium sulfate ($CaSO_4$) were purchased from Aladdin (China). PLGA (acid terminated, lactide:

glycolide 50 : 50, M_w 40 000) was obtained from Meilunbio (China). PLLA (M_w 260 000) was purchased from Daigang Biomaterial (China). Calcein-AM/PI double-labeled kit, Dulbecco's Modified Eagle's Medium (DMEM), PBS, DAPI, human β-NGF Elisa kit, fluorescent probe DCFH-DA, lipopolysaccharide (LPS), Vitamin B12 and Masson's trichrome staining kit were purchased from Solarbio (China). Collagenase type I, horse serum and fetal bovine serum were obtained from Gibco (USA), recombinant human β-NGF from Peprotech (USA), O.C.T. compound from Sakura (USA), mouse CD11c, CD206 and CD11b antibody from BioLegend (USA), mouse CD86 (sc52448) antibody from Santa Cruz (USA), rabbit CD163 (ab182422), NF200 (ab7794), S100 (ab52642) antibody, Goat Anti-Rabbit IgG H&L (Alexa Fluor® 488, ab150077), and Goat Anti-Mouse IgG H&L (Alexa Fluor® 647, ab150115) from Abcam (UK) and osmium tetroxide, epoxy resin, uranyl acetate and lead citrate from Sigma-Aldrich (USA). The SD rats and BALB/C mice were purchased from Beijing Vital River Laboratory Animal Technology Co. Ltd (China).

Preparation of NGF-loaded PLGA NPs

PLGA NPs were prepared using a $W_1/O/W_2$ emulsifying-solvent evaporation technique. Briefly, 5 mL of methylene chloride solution containing 375 mg of PLGA were mixed with 500 μL of aqueous solution containing 100 μg of NGF and 2 mg of bovine serum albumin (BSA). Then the mixture was emulsified by sonication for 5 min (ultrasound for 2 s, interval for 2 s, 360 W) under the conditions of circulating condensate water. The primary emulsion (W_1/O) was mixed with 30 mL of 1% PVA solution and emulsified by sonication again for 15 min using the same procedure. The oil phase was evaporated from the obtained $W_1/O/W_2$ emulsion with rotary evaporation. Finally, the obtained nanoparticles were washed and centrifuged at 10000 rpm 10 times. Before freeze drying, use a BeckMan Nanosizer (DelsaMax PRO, USA) to test the diameter of the NGF-loaded PLGA nanoparticles. The particles were observed by TEM (Tecnai G2, USA).

Preparation of NGF-loaded MSs

NGF-loaded PLGA NPs were mixed well with alginate solution (5% w/v) at a concentration of 2 mg mL^{-1}, then 200 μg of NGF powder and 1 mg of BSA was added into the solution. The mixture was vacuumed for 20 min to remove air bubbles and then transferred into a 5 mL syringe with a 25 G metal needle, then the syringe was placed into the electrospinning device. The negative electrode was connected to a receiving container with 50 mL $CaCl_2$ solution (5% w/v) and the positive electrode was connected to the metal syringe needle. The solution was sprayed toward the receiving container under high voltage (25 kV) and low voltage (−5 kV). Then the microspheres collected were washed and centrifuged 3 times with PBS. The bright field images were carried out with a stereomicroscope (SZX7, Olympus, Japan) for recording the morphology of microspheres. And the samples were frozen at −80 °C overnight and fixed onto the sample stage of a freezing microtome (CM3050S, Leica, Germany), then the particles were sliced to obtain a cross section for SEM observation. The obtained microspheres were stored at −20 °C for further experiments.

Preparation of the RCDDS

Nerve scaffolds need a preformed shell to contain the hydrogel and provide support for the broken nerve. We used an electrospinning method for the fabrication of the shell. PLLA was dissolved into hexafluoroisopropanol to make a 7.5% PLLA solution and transferred into a micro-injection pump with a 25 G mental needle, then 12 kV positive voltage was applied on the needle. The receiver was 20 cm away from the needle and rotated at 1000 rpm under a negative pressure of 3 kV. The spinning time is 30 minutes, the temperature is 30 °C and the humidity is 20%. Then the electrospinning film is dried in a vacuum drying oven for 8 hours at 60 °C. The film was gently rolled on a smooth cylinder with a diameter of 1.5 mm. A mixed solution of nitrogen dimethylformamide (DMF) and alcohol (99.9%) with a volume ratio of 1 : 20 was used at the tail end for adhesion. After drying in a vacuum drying oven for 12 hours at 60 °C, the preforming PLLA shells were obtained.

To make the main component of the RCDDS, alginate was purified through dialysis (3500 MW cut off) and lyophilization. We referred to the preparation method in ref. 41 for the next steps.[41] The dialyzed alginate was dissolved in 2-morpholinoethanesulphonic acid (MES) buffer (pH = 5) to make a 2.5 wt% alginate solution. Before mixing the NGF-loaded alginate MSs into the alginate solution, the MSs were dissolved in MES buffer. The final concentration of the MSs was 1 mg mL^{-1}. 4 mL of the above mixed solution were quickly mixed with 1 mL of 21 mg mL^{-1} $CaSO_4$ in water slurry by linking two 5 mL syringes together with a Luer Lock Connector and rapidly transferring the mixture back and forth between syringes. The reason why we chose calcium sulfate instead of calcium chloride as the cross-linking solution is that calcium sulfate is a slightly soluble system that can slowly release and crosslink during the cross-linking process, leading to the formation of a more complete cross-linking system.[41] Hydrogels were cast by quickly ejecting the contents of the syringes into the preforming porous PLLA shell. After gelation for 30 min, the calcium-crosslinked hydrogels-based RCDDS were obtained. For the micromorphology of the ultrasound-responsive hydrogel after stimulation with different ultrasound intensities, the hydrogels were simulated and frozen in liquid nitrogen immediately. After freeze drying, the materials were used for SEM observation.

Drug release behavior *in vitro*

The release of Vitamin B_{12} was tested using the method of ultraviolet spectroscopy, and the characteristic peak of Vitamin B_{12} is at 361 nm. 100 mg of RCDDS were weighted for each sample and were immersed in a sample bottle with 2 mL PBS and put at 37 °C in an incubator. 100 μL of the solution was used for the UV spectroscopy (Lambda 35, PerkinElmer, USA) test after different intensity ultrasound stimulation for 1, 2, 3, 5 and 7 days, and then an equal volume of fresh PBS was added into the sample bottle. For the NGF release study, a human β-NGF Elisa kit was used to determine the NGF concentration.

Neuron cell viability and axon regeneration evaluation

A cell study was carried out with PC-12 cells (ATCC CRL-1721). After culturing to a logarithmic growth stage, the PC-12 cells were seeded onto cell plates and co-cultured with the RCDDS at a density of 6×10^4 cells per mL. The PC-12 cells were then cultured in DMEM containing 10% horse serum, 5% fetal bovine serum, 100 U mL^{-1} of penicillin, 100 μg mL^{-1} of streptomycin, and 2 mM L-glutamine. The cells were maintained at 37 °C in a saturated humidity atmosphere with 95% air and 5% CO_2. To study the differentiation of PC-12 cells, 20 ng mL^{-1} of NGF was added to the cell medium.

A calcein-AM/PI double-labeled kit was used to stain the live/dead PC-12 cells. The cells were cultured for 3 days with the RCDDS under different intensities of ultrasound stimulation and detached from the(tissue cell plate) TCPs by using 0.25% trypsin-EDTA solution, collected into a centrifuge tube, and centrifuged at 1000 rpm for 5 min. Then the supernatant was removed and the cells were washed twice with 1× assay buffer. After adding a certain amount of Calcein-AM solution into the cells, the cells were incubated in the shade for 20–25 min at 37 °C. Then, the cells were stained with PI solution in the dark for 5 min at room temperature. After washing gently with PBS to remove the extra staining solution, the cells were visualized using a fluorescence microscope (DM6000, Leica, Germany) at 490 nm for live cells and at 545 nm for dead cells.

To test the effect of RCDDS under different ultrasound intensity to promote axon regeneration, 6 different groups were set (TCP, RCDDS, RCDDS with 0.1 W cm^{-2} US, RCDDS with 0.5 W cm^{-2} US, RCDDS with 0.8 W cm^{-2} US and RCDDS with 1 W cm^{-2} US). Briefly, PC12 cells were cultured in TCP with RCDDS or without RCDDS. After 3 days of culture and intervention, the cells were fixed and permeabilized, and the cytoskeleton was stained using phalloidin reagent for 30 min. Three additional washes were performed before the cells were counterstained with DAPI. Images were acquired using a fluorescence microscope (DM6000, Leica, Germany).

Anti-inflammation evaluation

For examination of the anti-inflammatory effect of VB_{12} released in the RCDDS, we employed lipopolysaccharide (LPS) treated RAW 264.7 cells to fabricate an inflammatory model. The cells were seeded on a 24-well plate and were divided into the control group, LPS (1 μg mL^{-1}) induced group (LPS), LPS and RCDDS treatment group (LPS + RCDDS), and LPS and RCDDS with ultrasound stimulation group (LPS + RCDDS + US). 2′,7′-Dichlorodihydrofluorescein diacetate (DCFH-DA) fluorescent probes was used to test the intracellular ROS level under different conditions. The supernatants of the cells were removed and 300 μL of diluted DCFH-DA (10 μmol L^{-1}) was added into the cells in each well. After incubating in a 37 °C incubator for 20 minutes, the cells were washed with cell culture medium three times and were digested using 0.25% trypsin and collected for flow cytometry. The determinations were performed in a cell quantitative analyzer (C6, BD Biosciences, USA) and analysed using FlowJo software.

We further used a mouse intramuscular model to test the immune response *in vivo* at the early stage of RCDDS implantation. Eighteen BALB/C mice (6 weeks, female) were used and randomly divided into two groups. After anesthesia, the sciatic nerves from the right leg of the mice were clipped and RCDDSs (3 mm) were implanted near the injured sciatic nerve for the experimental group, and only the sciatic nerve injury was implemented for the control group. At the indicated time points, to obtain macrophages, the mice were sacrificed, and the implanted RCDDS and tissue nearby were isolated and digested at 37 °C for 1 h with 0.2% collagenase D and 100 U mL^{-1} recombinant DNase I. The resulting cell suspension was filtered with a 40 μm millipore filter and washed with PBS. The cells were blocked with CD16/CD32 monoclonal antibody for 10 min at 4 °C, then the immune cells were stained with the following antibodies: PE-CD206, APC-CD11c and FITC-CD11b. Subsequently, the cells were analyzed by flow cytometry.

We also conducted immunofluorescent staining of the tissue near the implants. The tissues containing the RCDDS of the experiment group and tissues of the control group were separated from the mice, embedded in O.C.T. compound and frozen immediately in liquid nitrogen. The frozen tissues were cut into 10 μm section slices using a freezing microtome (CM3050S, Leica, Germany). Then the sections were fixed in 4% PFA for 10 min, permeabilized with 0.5% Triton X-100 for 10 min followed by blocking in 5% goat serum at room temperature for 40 min. Subsequently, the sections were incubated overnight at 4 °C with the antibodies CD86 (1 : 100) and CD163 (1 : 200). After washing with PBS, the sections were incubated with the secondary antibody, goat anti-rabbit IgG H&L (Alexa Fluor 488) and goat anti-mouse IgG H&L (Alexa Fluor 647) for 2 h at room temperature, then the sections were washed and stained with DAPI for 10 min. Finally, the sections were used for immunofluorescence observation under a laser scanning confocal microscope (SP8, Leica, Germany).

Animal surgery and treatment

All animal experiments were performed according to protocols approved by the Committee on Ethics of Beijing Institute of Nanoenergy and Nanosystems (A-2022018), and all animal procedures were carried out in line with the national standards of Laboratory Animal Requirements of Environment and Housing Facilities (GB14925-2001). Thirty adult female Sprague-Dawley (SD) rats (200–250 g) were randomly divided into six groups: the autograft group, AH_{VB12} + US group, NP-MS-AH_{NGF} + US group, RCDDS group, RCDDS + US and RCDDS + tun-US group. Animals were anesthetized using isoflurane and the right sciatic nerves were exposed. After routine skin preparation and disinfection, the right sciatic nerves were exposed and a 10-mm defect was created in the middle portion of the nerve trunk. The prepared scaffolds were used to bridge the gap and 1-mm segments of the proximal and distal nerve stumps were inserted into the conduit and sutured with a 9-0 suture. For the autograft control, the 10-mm nerve from the left sciatic nerve was reserved and re-bridged. After the rats were resuscitated from the anesthetization, they were housed in their cages as usual. Some groups were treated with ultrasound stimulation

every other day. For the blood routine examination, the tail vein blood of the rats was collected and stored in anticoagulant blood collection vessels, and then the levels of inflammatory cells in the blood were evaluated by using a blood cell analyzer (BC6600Plus, Mindray, China).

Morphometric analysis of nerve regeneration:

At 12 weeks post-surgery, the sciatic nerve tissues were harvested and fixed with 10% formalin overnight. The tissues were dehydrated with graded ethanol and embedded in paraffin blocks for sectioning (4 μm). After blocking with 3% BSA and 10% FBS in 0.3% Triton X-100 for 2 h at room temperature, the sections were incubated with Mouse monoclonal anti-Neurofilament antibody (NF200, 1:500) and Rabbit monoclonal anti-S100 antibody (1:200) overnight. Then the sections were treated with Goat Anti-Rabbit IgG H&L (Alexa Fluor 488) and Goat Anti-Mouse IgG H&L (Alexa Fluor 647) for 1 h. Finally, DAPI was used to stain the sections for 10 min. The images were taken and evaluated using a panoramic scanner (P250 Flash, 3DHISTECH, Hungary) and ImageJ, and each sample was evaluated in three random fields.

Morphological assessment of the myelinated axons of the regenerated nerve was performed with transmission electron microscopy (TEM, Tecnai Spirit 120 kV, FEI, USA). The rat was anesthetized and inserted with a perfusion needle into the left ventricle. After the beginning of perfusion, the auricula dextra of the rat was cut, and 40 mL of saline solution and 100 mL of 4% paraformaldehyde (PFA) and 2.5% glutaraldehyde (GA) solution were injected into the rat in order. The fixed sciatic nerves were incubated in 2.5% GA solution for 2 h in a shaker at room temperature, followed by being transferred to 4 °C overnight. Then the samples were treated with 1% osmium tetroxide for 2 h at room temperature, dehydrated through alcohol gradient with 50%, 70%, 80%, 90%, and 100% ethanol sequentially and embedded with epoxy resin. After being processed into ultrathin sections using a ultramicrotome (EM UC6, Leica, Germany), the samples were stained with uranyl acetate and lead citrate, and were observed with TEM to photograph the myelin sheaths of the regenerated nerves. The images were analyzed using ImageJ software for the thickness of the myelin sheaths and diameter of axons and 20 different myelins were evaluated for each group.

Animal functional recovery assessment and electrophysiological evaluation

The walking track analysis was performed to evaluate the restoration of locomotor function at 2, 4, 8 and 12 weeks after operation. The rats were led into the entrance of a narrow channel with their hind paws brushed with nontoxic black ink, and the footprints were registered on white paper covering the floor. Sciatic nerve function index (SFI), an indicator of locomotor nerve dysfunction, was scored using the following parameters:

$$\mathrm{SFI} = -38.3 \times \frac{\mathrm{EPL} - \mathrm{NPL}}{\mathrm{NPL}} + 109.5 \times \frac{\mathrm{ETS} - \mathrm{NTS}}{\mathrm{NTS}} + 13.3 \times \frac{\mathrm{EIT} - \mathrm{NIT}}{\mathrm{NIT}} - 8.8$$

Normal print length (NPL), normal toe spread (NTS), normal intermediary toe spread (NIT), experimental print length (EPL), experimental toe spread (ETS), and experimental intermediary toe spread (EIT).

The electrophysiological test was performed at 12 weeks after transplantation. The rats were anesthetized and the right sciatic nerves were exposed. A stimulating electrode (Cuff electrode, KedouBC, China) was placed across the nerve fiber 4 mm proximal to the injury site, the counter electrode was inserted into the subcutaneous tissue near the foot muscle and the ground electrode was placed in the rat away from the stimulation region. The electrophysiological recorder (Biopac MP150, USA) was used to record the compound muscle action potential (CMAP).

Morphometric analysis of the gastrocnemius muscle

After the rats were sacrificed, bilateral gastrocnemius muscles of all the groups were explanted immediately and the wet weight was recorded. Then the muscles were fixed and embedded in paraffin for sectioning. The sections were stained with a Masson's trichrome staining kit and examined with a light microscope (Nikon). The areas of blue collagen fiber of the photos were analysed using ImageJ software in three random fields for each section.

Statistical analysis

All results were statistically analysed and reported as means ± SD. The P value was determined using One-way ANOVA with Tukey's multiple comparison test ($^{*}P < 0.05$, $^{**}P < 0.01$, $^{***}P < 0.001$, $^{****}P < 0.0001$) with GraphPad Prism 8.0 software.

Data availability

Data supporting the results of this study can be obtained from the corresponding author upon request.

Author contributions

Y. S. and L. X. designed and conducted most of the experiments and analysed the data. Z. L., H. F., D. L., H. O. and Z. Y. designed and supervised the study. X. C. and J. L. collaborated to help in the animal experiments. E. W. and F. J. contributed to the material fabrication and characterization. Y. S., L. X. and D. L. wrote the manuscript. H. F., H. O., T. Y., D. L. and Z. L. reviewed and revised the manuscript. All authors discussed the results and approved the final manuscript.

Conflicts of interest

There are no conflicts to declare.

Acknowledgements

This work was financially supported by the National Key Research and Development Program of China (2022YFE0111700, 2022YFB3804703, 2021YFB3201200, 2022YFB3205602), the

National Natural Science Foundation of China (T2125003, 81971770, 52372174, 52002027), the Beijing Natural Science Foundation (JQ20038, L212010), the Fundamental Research Funds for the Central Universities (EOEG6802X2, E2E46806), and the General programs of the Natural Science Foundation of Hubei Province (2022CFB200).

Notes and references

1 R. Deumens, A. Bozkurt, M. F. Meek, M. A. E. Marcus, E. A. J. Joosten, J. Weis and G. A. Brook, *Prog. Neurobiol.*, 2010, **92**, 245–276.
2 A. D. Gaudet, P. G. Popovich and M. S. Ramer, *J. Neuroinflammation*, 2011, **8**, 110.
3 Y. Qian, H. Lin, Z. Yan, J. Shi and C. Fan, *Mater. Today*, 2021, **51**, 165–187.
4 P. Chen, X. Piao and P. Bonaldo, *Acta Neuropathol.*, 2015, **130**, 605–618.
5 W. R. Qu, Z. Zhu, J. Liu, D. B. Song, H. Tian, B. P. Chen, R. Li and L. X. Deng, *Neural Regener. Res.*, 2021, **16**, 93–98.
6 M. V. Sofroniew, C. L. Howe and W. C. Mobley, *Annu. Rev. Neurosci.*, 2001, **24**, 1217–1281.
7 V. M. Gaspar, P. Lavrador, J. Borges, M. B. Oliveira and J. F. Mano, *Adv. Mater.*, 2020, **32**, e1903975.
8 W. Xue, W. Shi, Y. Kong, M. Kuss and B. Duan, *Bioact. Mater.*, 2021, **6**, 4141–4160.
9 P. Lavrador, M. R. Esteves, V. M. Gaspar and J. F. Mano, *Adv. Funct. Mater.*, 2020, **31**, 2005941.
10 H. Xia, X. Li, W. Gao, X. Fu, R. H. Fang, L. Zhang and K. Zhang, *Nat. Rev. Mater.*, 2018, **3**, 174–193.
11 S. M. Willerth and S. E. Sakiyama-Elbert, *Adv. Drug Delivery Rev.*, 2007, **59**, 325–338.
12 P. J. Horner and F. H. Gage, *Nature*, 2000, **407**, 963–970.
13 A. Ehmedah, P. Nedeljkovic, S. Dacic, J. Repac, B. Draskovic-Pavlovic, D. Vucevic, S. Pekovic and B. B. Nedeljkovic, *Molecules*, 2020, **25**, 5426.
14 W. Chan, M. Almasieh, M.-M. Catrinescu and L. A. Levin, *Am. J. Pathol.*, 2018, **188**, 160–172.
15 I. Dey, N. Midha, G. Singh, A. Forsyth, S. K. Walsh, B. Singh, R. Kumar, C. Toth and R. Midha, *Glia*, 2013, **61**, 1990–1999.
16 O. Chaudhuri, J. Cooper-White, P. A. Janmey, D. J. Mooney and V. B. Shenoy, *Nature*, 2020, **584**, 535–546.
17 A. Xiong Gao, T. C.-X. Xia, M. Shing-Hung Mak, K. Kin-Leung Kwan, B. Zhong-Yu Zheng, J. Xiao, T. T.-X. Dong and K. W.-K. Tsim, *Food Funct.*, 2021, **12**, 11515–11525.
18 A. Ehmedah, P. Nedeljkovic, S. Dacic, J. Repac, B. Draskovic Pavlovic, D. Vucevic, S. Pekovic and B. Bozic Nedeljkovic, *Molecules*, 2019, **24**, 4615.
19 A. Miller, M. Korem, R. Almog and Y. Galboiz, *J. Neurol. Sci.*, 2005, **233**, 93–97.
20 F. Wu, K. Xu, L. Liu, K. Zhang, L. Xia, M. Zhang, C. Teng, H. Tong, Y. He, Y. Xue, H. Zhang, D. Chen and A. Hu, *Front. Pharmacol.*, 2019, **10**, 406.
21 E. Tamaddonfard, A. A. Farshid, F. Samadi and K. Eghdami, *Drug Res.*, 2014, **64**, 470–475.
22 K. Okada, H. Tanaka, K. Temporin, M. Okamoto, Y. Kuroda, H. Moritomo, T. Murase and H. Yoshikawa, *Exp. Neurol.*, 2010, **222**, 191–203.
23 T. Watanabe, R. Kaji, N. Oka, W. Bara and J. Kimura, *J. Neurol. Sci.*, 1994, **122**, 140–143.
24 Y. J. Lee, M. Y. Wang, M. C. Lin and P. T. Lin, *Nutrients*, 2016, **8**, 118.
25 P. Liu, J. Peng, G. H. Han, X. Ding, S. Wei, G. Gao, K. Huang, F. Chang and Y. Wang, *Neural Regener. Res.*, 2019, **14**, 1335–1342.
26 P. J. Murray, *Annu. Rev. Physiol.*, 2017, **79**, 541–566.
27 F. Fregnan, L. Muratori, A. R. Simoes, M. G. Giacobini-Robecchi and S. Raimondo, *Neural Regener. Res.*, 2012, **7**, 2259–2266.
28 G. Lu, Y. Xu, Q. Liu, M. Chen, H. Sun, P. Wang, X. Li, Y. Wang, X. Li, X. Hui, E. Luo, J. Liu, Q. Jiang, J. Liang, Y. Fan, Y. Sun and X. Zhang, *Nat. Commun.*, 2022, **13**, 2499.
29 R. Medzhitov, *Science*, 2021, **374**, 1070–1075.
30 L. Huang, B. Xia, X. Shi, J. Gao, Y. Yang, F. Xu, F. Qi, C. Liang, J. Huang and Z. Luo, *FASEB J.*, 2019, **33**, 8600–8613.
31 N. B. Fadia, J. M. Bliley, G. A. DiBernardo, D. J. Crammond, B. K. Schilling, W. N. Sivak, A. M. Spiess, K. M. Washington, M. Waldner, H.-T. Liao, I. B. James, D. M. Minteer, C. Tompkins-Rhoades, A. R. Cottrill, D.-Y. Kim, R. Schweizer, D. A. Bourne, G. E. Panagis, M. Asher Schusterman, F. M. Egro, I. K. Campwala, T. Simpson, D. J. Weber, T. Gause, J. E. Brooker, T. Josyula, A. A. Guevara, A. J. Repko, C. M. Mahoney and K. G. Marra, *Sci. Transl. Med.*, 2020, **12**, eaav7753.
32 A. Donsante, J. Xue, K. M. Poth, N. S. Hardcastle, B. Diniz, D. M. O'Connor, Y. Xia and N. M. Boulis, *Adv. Healthcare Mater.*, 2020, **9**, 2000200.
33 Y. He, F. Li, P. Jiang, F. Cai, Q. Lin, M. Zhou, H. Liu and F. Yan, *Bioact. Mater.*, 2023, **21**, 223–238.
34 X. Liu, D. Zou, Y. Hu, Y. He and J. Lu, *Tissue Eng., Part B*, 2023, **29**, 414–428.
35 D. Ventre, M. Puzan, E. Ashbolt and A. Koppes, *J. Neural Eng.*, 2018, **15**, 046013.
36 F.-Y. Yang, W.-W. Lu, W.-T. Lin, C.-W. Chang and S.-L. Huang, *Brain Stimul.*, 2015, **8**, 465–473.
37 W.-T. Lin, R.-C. Chen, W.-W. Lu, S.-H. Liu and F.-Y. Yang, *Sci. Rep.*, 2015, **5**, 9671.
38 A. R. Armiento, L. P. Hatt, G. Sanchez Rosenberg, K. Thompson and M. J. Stoddart, *Adv. Funct. Mater.*, 2020, **30**, 1909874.
39 O. Jeon, C. Powell, L. D. Solorio, M. D. Krebs and E. Alsberg, *J. Controlled Release*, 2011, **154**, 258–266.
40 Y. Li, J. Rodrigues and H. Tomas, *Chem. Soc. Rev.*, 2012, **41**, 2193–2221.
41 N. Huebsch, C. J. Kearney, X. Zhao, J. Kim, C. A. Cezar, Z. Suo and D. J. Mooney, *Proc. Natl. Acad. Sci. U. S. A.*, 2014, **111**, 9762–9767.